The gas curtain experimental technique and analysis methodologies

J. Kamm[1], W. Rider[1], P. Rightley[1], K. Prestridge[1],
R. Benjamin[1], P. Vorobieff[2]
[1]*Los Alamos National Laboratory, Los Alamos, USA*
[2]*University of New Mexico, Albuquerque, USA*

Abstract

The qualitative and quantitative relationship of numerical simulation to the physical phenomena being modeled is of paramount importance in computational physics. If the phenomena are dominated by irregular (i.e., nonsmooth or disordered) behavior, then pointwise comparisons cannot be made and statistical measures are required. The problem we consider is the gas curtain Richtmyer-Meshkov (RM) instability experiments of Rightley et al. [13], which exhibit complicated, disordered motion. We examine four spectral analysis methods for quantifying the experimental data and computed results: Fourier analysis, structure functions, fractal analysis, and continuous wavelet transforms. We investigate the applicability of these methods for quantifying the details of fluid mixing.

1 Introduction

Our principal experimental basis is the gas curtain Richtmyer-Meshkov experiment of Rightley et al. [13] This experiment involves impulsively accelerating a curtain of SF_6 with a Mach 1.2 shockwave and examining the subsequent fluid mixing driven by the deposition of baroclinic vorticity in the gas curtain. We simulate the experiment with the adaptive mesh code RAGE [1] and the research code CUERVO [11]. Both codes use Godunov-type methods, although they differ significantly in the details.

Both the experiment and the calculations produce complicated, disordered motion. Given the sensitive dependence on the initial conditions for these flows, one cannot perform pointwise comparison of the flowfields.

Therefore, we examine the data and results with generalized spectral analysis methods. In addition to the standard Fourier analysis, we calculate second-order structure functions, fractal analysis characteristics, and continuous wavelet transforms.

The experimental configuration is discussed in further detail in §2. A brief description of the codes is provided in §3. The analysis techniques are described in some detail in §4. Results are provided in §5, followed by a summary in §6.

2 The gas curtain Richtmyer-Meshkov experiment

The experiments referred to here have been described in detail in [13] and references therein. We will describe them briefly and focus on aspects that are relevant to our current discussion.

The experimental apparatus is a 5.5 m shock tube with a 75 mm square test section. The driver section is pressurized before the shot, and the rupturing of a polypropylene diaphragm produces a Mach 1.2 planar shock. In the test section, a vertical curtain of SF_6 is injected through a nozzle in the top, and removed through an exhaust plenum at the bottom. Interchangeable nozzles containing different contours impose perturbations on the cross section of the curtain, which has a downward velocity of $\sim$ 10 cm/s. A photograph of the experimental facility is shown in Fig. 1.

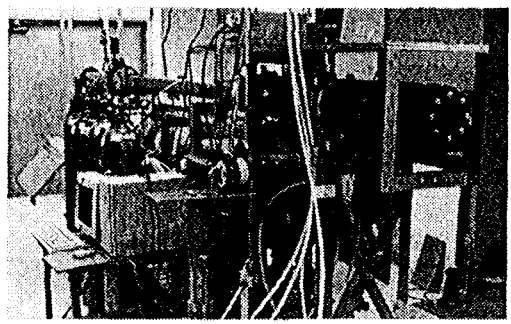

Figure 1: Photograph of the shock tube experimental facility in which the gas curtain experiments are performed.

The evolving flow is imaged by a horizontal laser light sheet. A tracer material consisting of glycol fog (with a typical droplet dimension of 0.5μm) is added to the curtain to greatly improve the dynamic range of the images, which are captured by CCD camera. A detailed discussion of the experimental apparatus, including a discussion of the flow tracking ability of the glycol fog and experimental error analysis, is given by Rightley *et al.* [13]

One aspect that is central to this work is the fidelity of the experimental images. Many high-speed flow instability experiments do not achieve the

image resolution that is obtained with the gas curtain apparatus. This resolution enables a substantive comparison of physical time and space scales with those computed. As a consequence, we seek to make deeper observations regarding the capacity of numerical simulations to model reality.

3 Numerical simulations

We use the images of the experimental initial conditions to initialize the computations. These images are corrected for noise by using a speckle filter that has a threshold intensity value equal to that of the CCD camera; the denoised images are used in the analysis of the experimental data. The denoised initial condition is subsequently smoothed with a Gaussian filter. These smoothed data are interpolated onto the computational grid, with the initial computational zone size equal to the pixel size of the image. We impose reflective boundaries at the top and bottom of the computational domain.

Our computations are done primarily with two hydrocodes: RAGE, an adaptive grid Godunov method [1], and CUERVO, a Godunov code for investigating more advanced algorithms [11]. Neither of these codes includes explicitly modeled viscous terms; however, preliminary simulations with equations containing viscous terms indicates no substantial difference in the computed results.

RAGE solves the Euler equations with an operator split Godunov method that is implemented in Lagrange-remap fashion with a linearized two-shock Riemann solver. The code has multimaterial capability with the assumption of local thermal, pressure, and momentum equilibrium. enforced. RAGE also has an adaptive mesh refinement (AMR) feature, which we used to allow the smallest computational zones to decrease to one-half the size of the initial condition, with the code output interpolated onto the original mesh.

CUERVO is a single material research code that is primarily used to investigate advanced numerical integration techniques. CUERVO uses unsplit differencing (both spatial and temporal) and an adaptive quadratic two-shock Riemann solver. CUERVO does not presently have genuine multimaterial capability. Additionally, other physics can be added to the code without difficulty, a case in point being the diffusive terms (or, *e.g.*, simple turbulence models).

4 Spectral analysis methods

Since pointwise comparison of the evolving unstable flow is not meaningful, we turn to spectral analysis techniques to quantify the sub-integral scale behavior. In all cases, we use measures with which we can directly compare *quantitatively*, over some range of length scales, experimental observations and computational results. We first briefly review Fourier analysis, then discuss structure functions, fractal analysis, and the continuous

wavelet transform, each of which provides a unique measure of the scale-dependent properties. The literature on each of these topics is voluminous; the references we cite are those that we have found to be most useful.

Fourier methods form the foundation of data and image analysis. We define the 2-D Fourier transform $\mathcal{F}$ of a function f and its inverse $\mathcal{F}^{-1}$ as

$$\mathcal{F}_f(k_x, k_y) \equiv \int_{-\infty}^{\infty} dx \int_{-\infty}^{\infty} dy \; f(x,y)\, e^{i2\pi k_x x}\, e^{i2\pi k_y y} \;=\; \hat{f}(k_x, k_y) \quad \text{with (1)}$$

$$\mathcal{F}_{\hat{f}}^{-1}(x,y) \equiv \int_{-\infty}^{\infty} dk_x \int_{-\infty}^{\infty} k_y \; \hat{f}(k_x, k_y)\, e^{-i2\pi k_x x}\, e^{-i2\pi k_y y}\,. \qquad (2)$$

We use the complex multidimensional NIST FFT package [9], which does not require that the number of data be a power of two. The spectral energy E and spectral energy density $\mathcal{E}$ (often called the "Fourier spectrum") are calculated as functions of the wavevector magnitude k according to

$$E(k) = \frac{1}{2} \sum_{|\mathbf{k}'|<k} |\hat{f}(\mathbf{k}')|^2 \quad \text{and} \quad \mathcal{E}(k) = \frac{d}{dk} E(k)\,. \qquad (3)$$

One often-cited Fourier spectrum result is for homogeneous, isotropic, incompressible turbulence in the limit of infinite-Reynolds number, for which the celebrated Kolmogorov scaling (so-called K41 theory) is $\mathcal{E}(k) \sim k^{-5/3}$ [4].

Perhaps the simplest statistical measure to calculate is the second order autocorrelation, *i.e.*, the second-order structure function. The second-order scalar structure function of the data f is defined as:

$$S_2(\ell) = \left\langle \left[f(\mathbf{x}_n + \boldsymbol{\ell}) - f(\mathbf{x}_n) \right]^2 \right\rangle \sim C\, \ell^{d_s}\,, \qquad (4)$$

where ℓ is the magnitude of vector $\boldsymbol{\ell}$, and the expectation operator $\langle \cdot \rangle$ is the sample mean. In this study, we compute the isotropic structure function, *i.e.*, we consider all orientations of the vector $\boldsymbol{\ell}$. We compute this quantity over a range of length scales, *i.e.*, for a range of ℓ; we then calculate the best-fit to the scaling exponent d_s in eqn (4), and compare data sets via these exponents.

Fractal analysis has been used extensively to characterize, both theoretically and experimentally, turbulent fluid phenomena [14]. Of the numerous ways to approximate the fractal dimension, we consider two: (1) box counting for a contour, and (2) the variation method for a surface.

For box counting [5], we consider a range of volume-fraction contours, and evaluate the fractal dimension of each contour. The following pseudocode algorithm approximates the fractal dimension d_{fb}.

```
Loop over all contour values f_m, m = 1,...,M
   Loop over all scales ℓ_l, l = 1,...,L
      Determine the minimum number of boxes N_m(ℓ_l), each
      of linear dimension l, required to cover the contour
   Compute a power law fit to N_m = C_m ℓ^{-d_fb}
```

There are subtle implementation details in determining whether a given contour value is contained in a given box. Additionally, calculating the *minimum* covering number of boxes can be computationally intensive, but is required to numerically approximate the fractal dimension. Also, the fractal dimension is rigorously defined as the value of the exponent d_{fb} in the limit of vanishingly small box size; obviously, this limit cannot be realized for digitized quantities of finite resolution.

The variation method [2] for computing the fractal dimension of a surface proceeds in an entirely different manner. For a given resolution ε_l, one first calculates the upper ($\overline{f}_l$) and lower ($\underline{f}_l$) envelopes of the data (f) in local ε_l-neighborhoods. The ε-variation $V(\varepsilon_l)$ is then computed as mean of the difference between these surfaces:

$$V(\varepsilon_l) = \frac{1}{A} \int_{x_{\min}}^{x_{\max}} dx \int_{y_{\min}}^{y_{\max}} dy \left[\overline{f}_l(x,y) - \underline{f}_l(x,y) \right] , \tag{5}$$

where $A = (x_{\max} - x_{\min})(y_{\max} - y_{\min})$. This quantity is scaled to give an approximation to the fractal dimension d_{fv}. The following pseudocode uses the "pyramid algorithm" of Dubuc *et al.* [2] to approximate the variation fractal dimension d_{fv} for a surface with topological dimension D:

```
Initialize:  f̄_1(i,j) = f(i,j),  f̲_1(i,j) = f(i,j)
Loop over the scale indices l = 2,...,L
   Loop over all points i = 1,...,N_i,  j = 1,...,N_j
      f̄'_l(i,j) = max{ f̄_{l-1}(i-1,j), f̄_{l-1}(i+1,j) }
      f̲'_l(i,j) = min{ f̲_{l-1}(i-1,j), f̲_{l-1}(i+1,j) }
   Loop over all points i = 1,...,N_i,  j = 1,...,N_j
      f̄_l(i,j) = max{ f̄'_l(i,j-1), f̄'_l(i,j+1) }
      f̲_l(i,j) = min{ f̲'_l(i,j-1), f̲'_l(i,j+1) }
   Approximate the integral as
      V(ε_l) ≈ Δx Δy Σ_{i=1}^{N_i} Σ_{j=1}^{N_j} [ f̄_l(i,j) - f̲_l(i,j) ]
Compute a power law fit to V = C ℓ^{D+1} ℓ^{-d_fv}
```

In this approach, the length of the lth scale is $\ell_l = 2l\Delta x$, where we assume that $\Delta x = \Delta y$; also, $D = 2$ for the case considered. This algorithm is more efficient than that for box counting, and is less complicated to code.

Our fractal analysis software has been verified against images of known fractal dimension. The calculated (global) fractal dimension depends strongly on the range of scales used in the power law fitting process. For example, the box-counting algorithm gives results for the Sierpinski gasket (with exact fractal dimension $\log 3/\log 2 \doteq 1.585$) of between 1.53 and 1.58. Similarly, the variation dimension results for a discrete fractal Brownian motion surface of known dimension 2.6 vary between 2.45 and 2.64.

As these verification results suggest, numerical approximations to the fractal dimension suffer from a number of shortcomings [6]. For example,

the result can be biased by the nature of the curve fitting; therefore, one can calculate the *local* fractal dimension, which is the scaling exponent between each pair of box sizes/length scales data, *i.e.*, the local log-log slope. Such complications do not prevent fractal analysis from being useful as a *quantitative* measure with which to compare images of data or numerical results that contain complex structure.

The continuous wavelet transform (CWT) [3] is a spectral technique in which a given function or data set is projected onto dilated and translated versions of a basis function, known as the "mother wavelet". The CWT has many applications in image processing, including, *e.g.*, quantification of images of turbulent flows [3, 15]. The CWT method differs from the *discrete* wavelet transform (DWT) method [10], which has widespread application in signal processing, including, *e.g.*, image compression.

The CWT of the function $f(\mathbf{x}) \equiv f(x,y)$ is defined as

$$W_{f,\psi}(a,b_x,b_y) = \frac{1}{a}\int_{-\infty}^{\infty} dx \int_{-\infty}^{\infty} dy\, f(x,y)\,\psi\left(\frac{x-b_x}{a},\frac{y-b_y}{a}\right), \qquad (6)$$

where ψ is the mother wavelet, a is the scale, and $\mathbf{b} = (b_x, b_y)$ is the (2-D) translation. The set of admissible mother wavelets must satisfy both

$$\int_{-\infty}^{\infty} dx \int_{-\infty}^{\infty} dy\ \psi(x,y) = 0 \quad \text{and} \quad \int_{-\infty}^{\infty} dx \int_{-\infty}^{\infty} dy\ |\psi(x,y)|^2 = 1\,. \qquad (7)$$

Because of these constraints, the CWT characterizes *local* behavior, unlike the Fourier transform, which quantifies *global* (or *periodic*) characteristics. The mother wavelet we consider is the isotropic Marr or "Mexican hat" wavelet given by $\psi(x,y) = (2-r^2)\exp(-r^2/2)/\sqrt{2\pi}$, where $r^2 \equiv x^2 + y^2$.

The CWT is basically a generalized convolution between the function of interest and a scaled version of the mother wavelet. We evaluate the CWT by using Fourier transforms, starting with the definition given in eqn (6), which is easily manipulated to obtain:

$$W_{f,\psi}(a,\mathbf{b}) = \frac{1}{a}\int_{\mathbb{R}^2} d\mathbf{k}\ \Psi(k)\,\hat{f}(-\mathbf{k})\,e^{-i2\pi\mathbf{k}\cdot(-\mathbf{b})}\,, \qquad (8)$$

where $\Psi(\mathbf{k})$ is the Fourier transform of $\psi(\mathbf{x}/a)$. Therefore, the 2-D CWT with scale a and translation $-\mathbf{b}$ can be written

$$W_{f,\psi}(a,-\mathbf{b}) = \frac{1}{a}\int_{\mathbb{R}^2} d\mathbf{k}\ \Psi(\mathbf{k})\,\hat{f}(-\mathbf{k})\,e^{-i2\pi\mathbf{k}\cdot\mathbf{b}} = \frac{1}{a^{1/2}}\,\mathcal{F}^{-1}_{\Psi\cdot\hat{f}}(\mathbf{b})\,, \qquad (9)$$

where, for the last equality, we have assumed that f is an even function, so that $\hat{f}(\mathbf{k}) = \hat{f}(-\mathbf{k})$, which is the Fourier transform of $f(-\mathbf{x})$. The *wavelet energy spectrum* $\tilde{E}_f$ [3] can be defined in terms of the CWT as

$$\tilde{E}_f(a) = \frac{1}{C_{\psi,f}}\int_{\mathbb{R}^2} d\mathbf{b}\ a^{-2}\,|W_{f,\psi}(a,\mathbf{b})|^2 \quad \text{with} \quad C_\psi \equiv \int_{\mathbb{R}^{2+}} d\mathbf{k}\ |\mathbf{k}|^{-2}\,|\hat{\psi}(\mathbf{k})|^2\,. \qquad (10)$$

The following pseudocode algorithm for evaluating the CWT of a scalar function of two arguments for isotropic mother wavelets is based on eqn (9).

```
FFT the data, obtaining f̂(−k_{x_i}, −k_{y_j})
Assign and loop over all scales a_l, l = 1,...,L
   Loop over all points i = 1,...,N_i, j = 1,...,N_j
     Assign the scaled wavelet ψ(x_i/a_l, y_j/a_l)
   FFT the scaled wavelet to obtain Ψ(k_{x_i}, k_{y_j})
   Calculate the wave-space product Ψ(k_{x_i}, k_{y_j}) f̂(−k_{x_i}, −k_{y_j})
   Inverse-FFT and rescale to obtain W_{f,ψ}(a_l, −b_{x_i}, −b_{y_j})
Compute spectra
```

The smallest scale a_1 cannot be less than the zone size of the input data, which are required to be on a uniform grid. Similarly, the largest scale a_L cannot exceed the extent of the input grid.

There are subtle implementation considerations, regarding, *e.g.*, aliasing, frequency resolution, etc.; see [7] for a discussion of these topics as related to the CWT. One important implementation detail is that the argument of the data (*i.e.*, (x_i, y_j)) and the argument of the scaled wavelet (*i.e.*, $(x_i/a_l, y_j/a_l)$) *must be* at the appropriate values for correct computation of the discrete (*i.e.*, FFT-based) convolution.

5 Results

The initial volume fraction and the volume fraction at $400\mu s$ after shock impact are shown in Fig. 2, which shows the experiment and two simulations. This figure reveals qualitative differences that are quantified with the application of the analysis techniques described above.

In the following, we provide examples of these quantification measures for the $t = 400\mu s$ volume fraction shown in Fig. 2. In each plot, the exper-

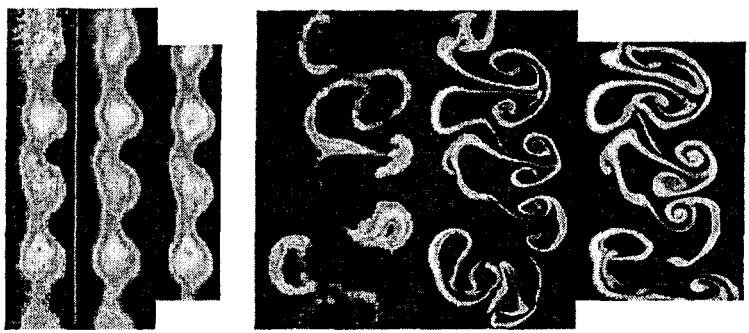

Figure 2: The SF_6 volume fraction pre-shock state (left) and at $400\mu s$ after shock impact (right). In each set, the experiment is shown on the left, the RAGE calculation in the middle, and the CUERVO calculation on the right.

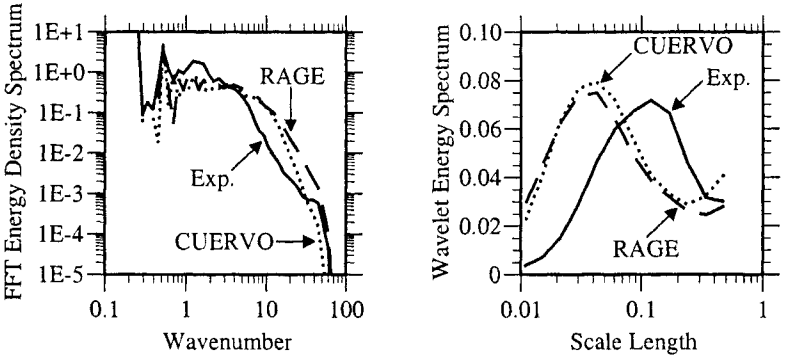

Figure 3: Left: the FFT energy density spectrum of the SF_6 volume fraction at 400μs. Right: the CWT energy spectrum of the SF_6 volume fraction at the same time.

imental result is a solid line, the RAGE calculation a dashed line, and the CUERVO calculation a dotted line.

Figure 3 contains plots of the Fourier spectrum, eqn (3), as a function of wavenumber k (left) and the CWT spectrum, eqn (10), as a function of scale length a (right) for the experiment and calculations. The CWT spectrum clearly reveals differences between the calculations (which have similar CWT spectra) and the experiment, as well as identifying different "dominant" length scales, *i.e.*, scales at which the (wavelet-dependent) energy of the flow is locally maximized. The FFT spectrum provides a less clear quantification of the flows. The FFT results, however, do indicate a lower energy density in the experiment at intermediate wavenumbers; this result is consistent with (although less illuminating than) the CWT results.

The second-order isotropic structure function, eqn (4) is shown as a function of length scale in Fig. 4. This plot suggests differences in the ranges of length scale over which (approximate) self-similar behavior occurs; such behavior is manifest as a straight line on this log-log plot. Fitting a power law curve to these results on the interval up to $\ell = 0.1$ quantifies these scaling variations: for the experiment $d_s = 1.36$,for the RAGE calculation $d_s = 0.75$, and for the CUERVO calculation $d_s = 0.87$.

Figure 5 contains plots of the box-counting fractal dimension for a range of contours (left) and the *local* variation fractal dimension for a range of scales (right). The error bars in the box-counting results are the standard deviations obtained from fitting the power-law *Ansatz*. For the box-counting results, there is statistically significant difference between experiment and calculation at all but the highest volume fraction contours; moreover, the results for the two calculations are again similar. The local variation dimension values exhibit a significant divergence of the experimental values from both calculated results over virtually the entire range of length scales.

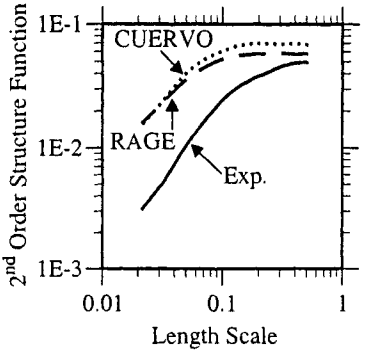

Figure 4: The second-order isotropic structure function versus length scale for the SF_6 volume fraction at $400\mu s$.

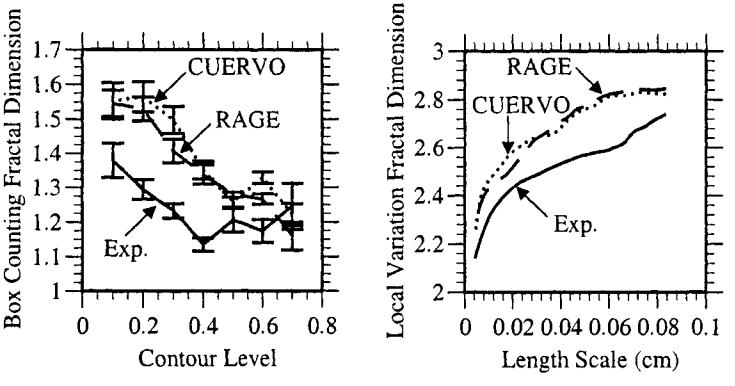

Figure 5: Left: the box-counting fractal dimension for a range of contours of the SF_6 volume fraction at $400\mu s$. Right: the local variation fractal dimension for a range of local scales at the same time.

6 Summary

The gas curtain experiment provides experimental data with which to examine sub-integral scale features of the Richtmyer-Meshkov instability in compressible flows. We presented measures–Fourier analysis, isotropic structure functions, fractal analysis, and continuous wavelets–with which to quantify the complicated mixing structures in this flow. We demonstrated that these methods are useful for quantifying numerical simulations of this experiment. These measures exhibit significant difference between calculated results and experimental data, with different dominant length scales (shown by the continuous wavelets) and different scaling behavior (shown by the structure function and fractal analyses). In a companion paper [12], we use these techniques to quantify, compare, and evaluate the effects of different numerical algorithms on the computed results.

Acknowledgement

This work is available as Los Alamos National Laboratory report LA-UR-01-497, and was performed at Los Alamos National Laboratory, which is operated by the University of California for the United States Department of Energy under contract W-7405-ENG-36.

References

[1] R. M. Baltrusaitis, M. L. Gittings, R. P. Weaver, R. F. Benjamin & J. M. Budzinski, Simulation of Shock Generated Instabilities, *Phys. Fluids*, **8**, pp. 2471–2493, 1996.

[2] B. Dubuc, S. W. Zucker, C. Tricot, J. F. Quiniou & D. Wehbi, Evaluating the fractal dimension of surfaces, *Proc. Roy. Soc. Lond. A*, **425**, pp. 113–127, 1989.

[3] M. Farge, Wavelet Transforms and Their Applications to Turbulence, *Ann. Rev. Fluid Mech.* **24**, pp. 395–457, 1992.

[4] U. Frisch, *Turbulence: The Legacy of A.N. Kolmogorov,* Cambridge University Press, Cambridge, pp. 57–71 and 89–91, 1996.

[5] G. Gonzato, A Practical Implementation of the Box Counting Algorithm, *Computers & Geosciences*, **24**, pp. 85–100, 1998.

[6] Q. Huang, J. R. Lorch & R. C. Dubes, Can the Fractal Dimension of Images be Measured?, *Pattern Recognition*, **27**, pp. 339–349, 1994.

[7] D. Jordan, R. W. Miksad & E. J. Powers, Implementation of the continuous wavelet transform for digital time series analysis, *Rev. Sci. Instrum.*, **68**, pp. 1484–1494, 1997.

[8] J. Lewalle, "Three Lectures on the Application of Wavelets to Experimental Data Analysis", VKI Lecture Series Notes 1998, available at `ftp.mame.syr.edu` in subdirectory `/pub/jlewalle`.

[9] Information regarding the NIST FFT software package is available at `http://www.netlib.org/go/`.

[10] R. M. Rao & A. S. Bopardikar, *Wavelet Transforms: Introduction to Theory and Applications,* Addison-Wesley, Reading, MA, pp. 25–50, 1998.

[11] W. J. Rider, An Adaptive Riemann Solver Using a Two-Shock Approximation, *Comp. Fluids*, **28**, pp. 741–777, 1999.

[12] W. Rider, J. Kamm, P. Rightley, K. Prestridge, R. Benjamin & P. Vorobieff, Direct Statistical Comparison of Hydrodynamic Mixing Experiments and Simulations, *this volume.*

[13] P. M. Rightley, P. Vorobieff, R. Martin & R. F. Benjamin, Experimental-Observations of the Mixing Transition in a Shock-accelerated Gas Curtain, *Phys. Fluids*, **11**, pp. 186–200, 1999.

[14] K. R. Sreenivasan, Fractals and Multifractals in Fluid Turbulence, *Ann. Rev. Fluid Mech.*, **23**, pp. 539–600, 1991.

[15] G. Treviño & E. L. Andreas, On Wavelet Analysis of Nonstationary Turbulence, *Boundary-Layer Meteorology,* **81**, pp. 271–288, 1996.